

# Investigation on Precipitation Behavior and Morphology of TiN Particles in High-Ti Low-Carbon High-Strength Steel

Wen Liang<sup>1,2</sup> · Run Wu<sup>1</sup> · Qing Yuan<sup>1,3</sup> · Jun Hu<sup>2</sup>

Received: 9 May 2019 / Accepted: 24 September 2019 / Published online: 11 November 2019  
© The Indian Institute of Metals - IIM 2019

**Abstract** The precipitation behavior of TiN particles under homogeneous and heterogeneous nucleation conditions in a low-carbon high-strength steel with 0.11 wt% Ti was investigated by thermodynamics and dynamics equations combining with the microstructural observations on the surface and at the core of the casting slabs. The effect of cooling rate on the morphology and dimension of TiN particles was also analyzed in the present study. In addition, the three-dimensional and the spatial tridimensional morphology of compound TiN–Al<sub>2</sub>O<sub>3</sub> was innovatively characterized by a focused ion beam scanning electron microscope. It was found that TiN particles possessed inerratic facet morphology (such as squares and clusters), and the square morphology was predominant. The preferential plane for TiN precipitates in the tested steel was {100}. Moreover, TiN particles precipitated both in solid and liquid phases from the solid–liquid phase region during

the solidification process, and preferential precipitation was observed in the solid phase. Furthermore, the size of TiN particles decreased with the increasing cooling rate during the casting process. Al<sub>2</sub>O<sub>3</sub> particles provided nucleation sites for the heterogeneous nucleation of TiN particles.

**Keywords** TiN inclusions · High-strength steel · Thermodynamics · Dynamics · Tridimensional morphology

## 1 Introduction

Titanium nitride (TiN) is a common inclusion in steels and possesses a face-centered cubic crystal structure with a lattice constant ( $a_0$ ) of 0.431–0.432 nm; thus, it generally appears in a regular cubic shape in steel products. The lattice mismatch between small-sized TiN and  $\delta$ -Fe is 3.9% at 1538 °C [1]. TiN precipitations at high temperatures act as the heterogeneous nucleation core of the primary  $\delta$ -ferrite phase and refine the initial solidified microstructure and improve the quality of steels [2–5]. The chemical stability of TiN is very high (melting point of 2930 °C); thus, it is very difficult to wipe TiN particles off by reactions with other elements once they are formed in steel samples. The element Ti comes from the low-carbon ferrotitanium alloy added during the vacuum treatment after deoxidization. However, the N comes from both the residuals in the molten iron and the N adsorption in the environment during steel tapping. And TiN forms gradually during the steelmaking process. Moreover, the elastic modulus of TiN is  $\sim$  600 GPa, which is much higher than that of the matrix steel ( $\sim$  200 GPa) [6]. The appearance of large-sized TiN particles exerts deteriorative effects on mechanical properties of steels. It is proved that the effects of 6  $\mu$ m-sized nitride inclusions on fatigue properties of

✉ Run Wu  
runwu@wust.edu.cn

Wen Liang  
e80179@baosteel.com

Qing Yuan  
yuanqing@wust.edu.cn

Jun Hu  
hujun\_jay@baosteel.com

<sup>1</sup> The State Key Laboratory of Refractories and Metallurgy, Key Laboratory for Ferrous Metallurgy and Resources Utilization of Ministry of Education, Wuhan University of Science and Technology, Wuhan 430081, China

<sup>2</sup> Wuhan Branch of Baosteel Central Research Institute, Wuhan 430080, Hubei, China

<sup>3</sup> Jiangsu Huaneng Cable Company Limited, Gaoyou 225613, Jiangsu, China

steels are equivalent to those of 25  $\mu\text{m}$ -sized oxide particles [7]. The TiN cloud acts as the cleavage fracture source under stresses and impairs the impact toughness and the fatigue life of steels [8–14]. Furthermore, it also exerts infaust effects on the whole expanding performance [15] and the drawing performance of steels [16, 17] during the forming process. Therefore, the volume fraction and the size of TiN particles are often decreased by reducing the contents of titanium (Ti) and nitrogen (N) in steels [18, 19]. On the other hand, the carbides of Ti provide precipitation and grain refinement strengthening in low-carbon high-strength microalloyed steels [1, 20–22]. In recent years, the sustainable development strategy has attracted considerable attention in iron and steel industries. With the development of microalloyed steels, an obvious shortcoming of high production cost due to the high price of microalloying elements in international markets has been exposed; thus, a strong trend of employing more Ti during steel production has emerged due to the relatively low price of Ti ore (in comparison to Nb and V) and the excellent strength–ductility balance of Ti-microalloyed steels. Some studies on Ti alloyed steels or Ti-containing composite microalloyed steels have been carried out. These studies mainly focus on microstructures and mechanical properties of microalloyed steels [23, 24], the deformation-induced ferrite transformation [25, 26] and heat treatment processes for microalloyed steels [27]. In addition, very few studies reported the formation mechanism and the morphologies of TiN particles [2, 28, 29]. However, it is well known that the micro-cracks preferentially form within the TiN particles, especially at the interface between the TiN housing and its heterogeneous nucleated core. The probability of cracking increases with the increase in dimension and volume fraction of TiN particles. Therefore, it is important to consider the precipitation behavior of TiN particles.

Nevertheless, investigations on high-Ti steels (Ti > 0.10 wt%) mixed with other microalloying elements are very limited. The precipitation behavior and the microstructural characterization of TiN in high-Ti steels are rarely reported. The novelty of present study is to clarify the precipitation behavior of TiN particles under homogeneous and heterogeneous nucleation conditions by thermodynamic and dynamic equations combining with the microstructural observations on the surface and at the core of the casting slabs. The effect of cooling rate on the morphology and dimension of TiN particles was also analyzed. Moreover, the three-dimensional and the spatial tridimensional morphologies of TiN were revealed by a focused ion beam scanning electron microscope (FIB-SEM). The obtained results could provide a better understanding on the precipitation behavior of TiN particles and important reference for the production of high-strength high-Ti-microalloyed steels.

## 2 Experimental Procedure

The chemical composition of the experimental low-carbon high-strength steel was 0.056C–0.05Si–1.40Mn–0.010P–0.0060S–0.030Nb–0.114Ti–0.0021N–0.034Al–balance Fe (in wt%). The specimens taken from the surface and the core of a continuous casting slab (thickness of 210 mm) were prepared to perform the microstructural characterization of TiN particles. Metallographic observations were carried out on an FEI Quanta 400 SEM to measure the size of TiN particles. In order to reveal the three-dimensional morphologies of TiN particles, a Zeiss Aurig FIB-SEM was employed. In addition, the chemical composition of TiN particles was analyzed by selected area elemental mapping through energy dispersive spectroscopy (INCA-EDS) at an operating voltage of 200 kV. The acquisition time was long enough to ensure sufficient acquisition counts. Film specimens for FIB-SEM were electrolyzed in 6 vol% perchloric acid–alcohol solution. Furthermore, the spatial tridimensional morphologies of TiN particles were also observed. Specimens were electrolyzed with a current of 20 mA/cm<sup>2</sup> in a solution of 1.0 vol% citric acid and 7.5 vol% potassium chloride. Ultrasonic processing, filtering, magnetic separation, rinsing, and drying were performed orderly after electrolysis, and the residues were used to observe the spatial tridimensional morphologies of TiN particles.

## 3 Results and Discussion

### 3.1 Homogeneous Nucleation

During the solidification of liquid metals, the main formation mechanisms of TiN particles are the homogeneous and heterogeneous nucleations. In the present research, the precipitation behavior of TiN particles under two nucleation modes has been separately studied. The liquidus ( $T_L$ ) and the solidus temperatures ( $T_S$ ) of the tested steel are calculated by Eqs. (1) and (2) [7, 28, 30]:

$$T_L = T_m - \sum_i m_i \times [\%i]_0 \quad (1)$$

$$T_S = T_m - \sum_i n_i \times [\%i]_0 \quad (2)$$

The relationship between temperature and solidification percentage is obtained by Eq. (3) [30]:

$$T = T_m - \frac{T_m - T_L}{1 - f_s} \cdot \frac{T_L - T_s}{T_m - T_L} \quad (3)$$

where  $T_m$  is the melting point temperature of pure iron (= 1809 K),  $m_i$  and  $n_i$  are the decrease in liquidus and

solidus temperatures, respectively, per 1% increase in the element *i* of liquid steel,  $[\%i]_0$  is the initial component of the element *i* in liquid steel (in wt%), and  $f_s$  is the solidification rate. The corresponding physical parameters of *m* and *n* can be found in the literature [31–33]. Therefore, the values of  $T_L$  and  $T_S$  for the tested steel are calculated as 1797 K and 1745 K, respectively. The concentration product ( $K_{I(TiN)}$ ) of TiN in the liquid phase is calculated by Eq. (4):

$$\lg K_{I(TiN)} = \lg([\% Ti]_l) + \lg([\% N]_l) = -\frac{14844}{T} + 5.56 \tag{4}$$

The concentration diagram of Ti and N at the liquidus temperature is displayed in Fig. 1. In the current smelting technology, the low content of N (0.0020–0.0060 wt%) has been controlled by the vacuum treatment to ensure the purity of molten steel. If TiN precipitates from the liquid phase, the initial content of N should be equal to or larger than 0.332 wt%. Hence, TiN can not directly precipitate from the pure liquid phase of the tested steel.

When the temperature of the molten steel decreases to the solid–liquid phase region, Ti and N begin to segregate. Scheil [34] calculated the element contents in liquid and solid phases during the solidification process by considering a fully diffusion and a diffusionless transformation of elements in the liquid and solid phases, respectively.

$$[\%i]_l = [\%i]_0 \cdot (1 - f_s)^{k_i - 1} \tag{5}$$

$$[\%i]_s = k_i [\%i]_0 \cdot (1 - f_s)^{k_i - 1} \tag{6}$$

where  $[\%i]_l$  and  $[\%i]_s$  are the mass fractions of the element *i* in the liquid and the solid phases during the solidification process,  $[\%i]_0$  is the mass fraction of the element *i* at the beginning of the solidification process,  $k_i$  represents the equilibrium solute partition coefficient of the element *i* [31–33]. The actual concentration product ( $Q_{I(TiN)}$ ) in the

liquid phase during the solidification process is calculated by Eq. (7):

$$Q_{I(TiN)} = [\%Ti]_l \cdot [\%N]_l = [\%Ti]_0 \cdot (1 - f_s)^{k_{Ti} - 1} \cdot [\%N]_0 \cdot (1 - f_s)^{k_N - 1} \tag{7}$$

Now, by combining Eqs. (4) and (7), the relationships among  $\lg Q_{I(TiN)}$ ,  $\lg K_{I(TiN)}$ , and  $f_s$  in the liquid phase are expressed in Fig. 2a. Similarly, the relationship among  $\lg Q_{S(TiN)}$ ,  $\lg K_{S(TiN)}$ , and  $f_s$  in the solid phase is also obtained (Fig. 2b). It is found that when  $\lg Q_{I(TiN)} > \lg K_{I(TiN)}$ , the precipitation thermodynamics of TiN from the solid and the liquid phases is met during the solidification process. When  $f_s$  is equal to 0.70 or 0.165, TiN separately precipitates from the liquid and the solid phases in the nonhomogeneous solid–liquid phase region. For high-strength steel with  $[\%Ti]_0 \geq 0.108\%$  and  $[\%N]_0 < 2.6 \times 10^{-5}\%$ , TiN does not precipitate in the liquid phase during solidification. However, it is very hard to control such low N content in the present smelting technology.

TiN is spontaneously precipitated in the liquid and the solid phases during the solidification. The growth of TiN in the liquid and solid phases can be determined in advance. The initially precipitated TiN particles in the molten steel are spherical in shape, and the diffusion of N is the controlling condition for the growth of TiN [35]. The growth of TiN particles in the liquid phase during solidification process is described by Eq. (8) [36]:

$$\frac{rdr}{dt} = \frac{M_s \rho_m}{100 M_m \rho_s} D_1 (C_1 - C_e) \tag{8}$$

where *r* is the radius of TiN particles (m), *t* is solidification time (s) and is calculated as  $t = (T_L - T_S)/R_c$ ,  $R_c$  is the cooling rate (K/s),  $M_m$  and  $M_s$  are the atomic weights of pure iron (0.056 kg/mol) and TiN (0.062 kg/mol), respectively,  $\rho_m$  and  $\rho_s$  are the densities of steel (7070 kg/m<sup>3</sup>) and TiN (5430 kg/m<sup>3</sup>), respectively,  $D_1$  is the diffusion coefficient of N in the molten steel and is equal to  $3.25 \times 10^{-7} \exp^{-11,500/RT}$  (m<sup>2</sup>/s),  $C_1$  is the actual content of N at the solidification front (%), and  $C_e$  is the actual content of N at the equilibrium state of TiN (%). Figure 3 presents the relationship between *r* and  $[\%Ti]_0$  and also between  $[\%N]_0$  and  $R_c$  based on Eq. (8). It is noticeable that the size of TiN changes with the cooling rate and the initial contents of Ti and N. Further, for the same  $f_s$ , the size of TiN increases with the increase in initial contents of Ti and N and the decrease in cooling rate. Moreover, the size of micron-scale TiN particles in the liquid phase reaches 30 μm.

The diffusion coefficient of N in the solid phase is much higher than that of Ti; thus, the precipitation of TiN in the solid phase is controlled by the diffusion of Ti. The diffusion coefficient ( $D_{S(Ti)}$ ) of Ti is equal to

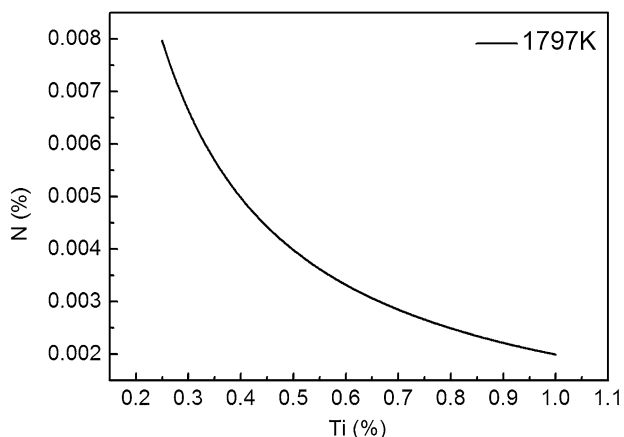


**Fig. 1** Relationship between the concentration of Ti and N in the liquid phase

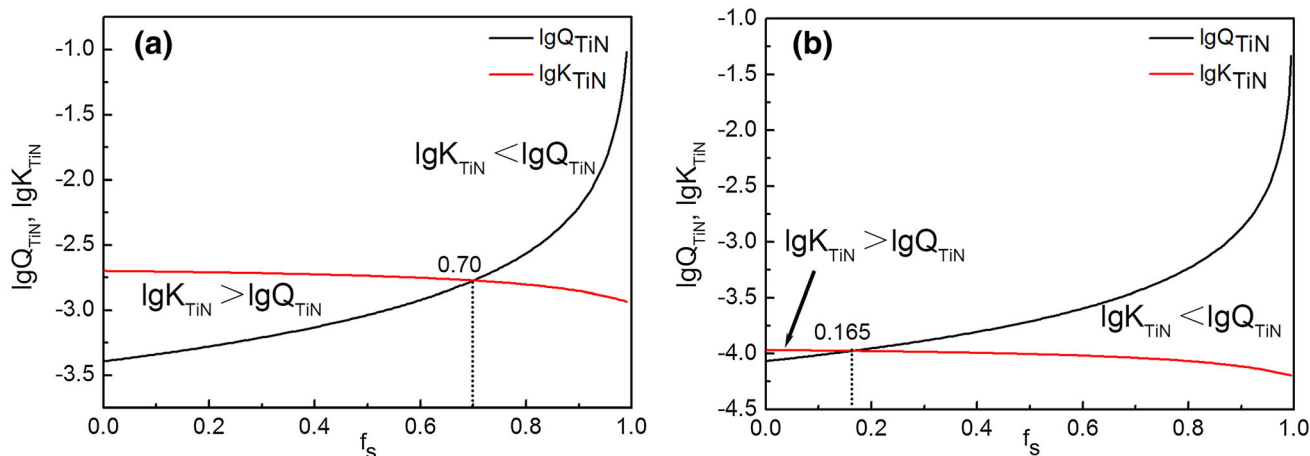


**Fig. 2** Relationship between  $\lg Q_{\text{TiN}}-f_s$  and  $\lg K_{\text{TiN}}-f_s$  in **a** liquid phase and **b** solid phase

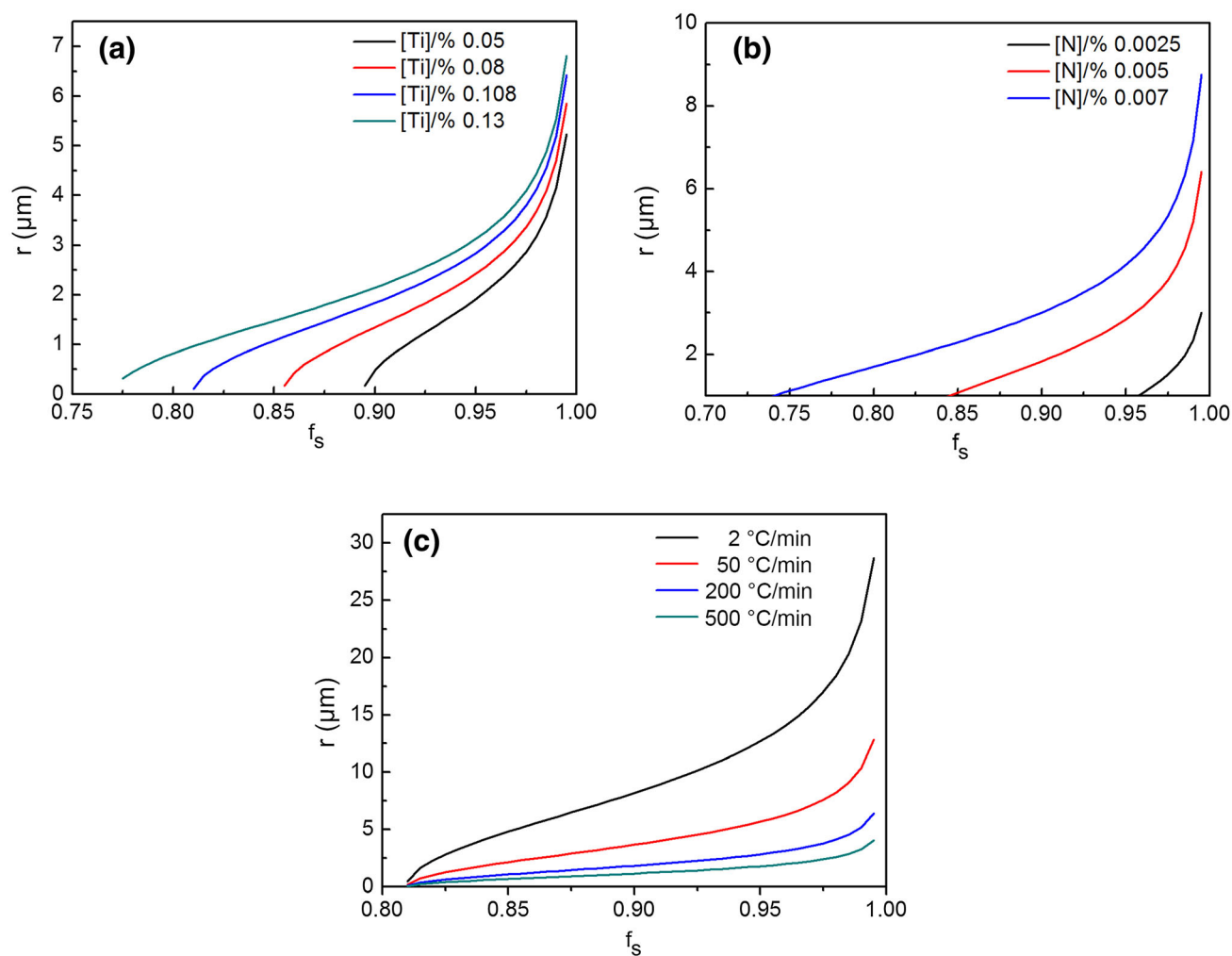


**Fig. 3** Relationship between size of TiN and **a** Ti content ( $R_C = 200$  °C/min,  $[\%N]_0 = 0.005\%$ ), **b** N content ( $R_C = 200$  °C/min,  $[\%Ti]_0 = 0.108\%$ ) and **c** cooling rate ( $[\%Ti]_0 = 0.108\%$ ,  $[\%N]_0 = 0.005\%$ )

$1.5 \times 10^{-5} \times \exp(-250,000/RT)$  ( $\text{m}^2/\text{s}$ ) [36], and the diffusion coefficient ( $D_{\text{I(N)}}$ ) of N in the molten steel at the solidification front is  $3.25 \times 10^{-3} \times \exp(-11,500/RT)$

( $\text{m}^2/\text{s}$ ). Figure 4 illustrates the relationship between  $\lg D$  and  $T$ . It is noticeable that  $D_{\text{I(N)}}$  is larger by 9–13 orders of magnitude than  $D_{\text{s(Ti)}}$ ; hence, it indicates that the

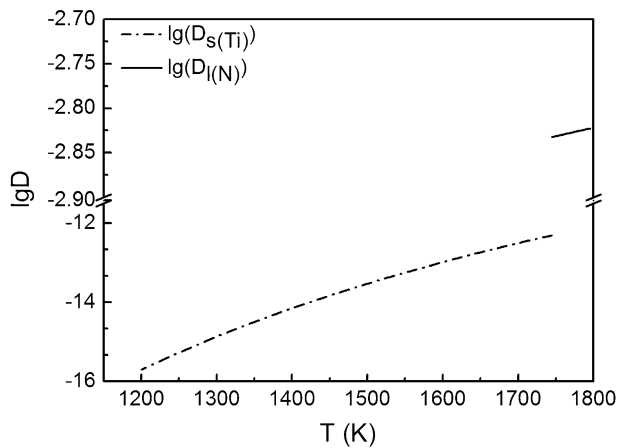


**Fig. 4** Relationship between the diffusion coefficient of the controlled element and the temperature during the TiN growth

growth rate of TiN particles in the liquid phase is much higher than that in the solid phase. Therefore, the growth rate and the final size of TiN particles in the solid phase are unmentioned.

### 3.2 Heterogeneous Nucleation

The critical nucleation radii for homogeneous and heterogeneous nucleations ( $r_{ho}^*$  and  $r_{he}^*$  respectively) are expressed by Eqs. (9) and (10) [37]:

$$r_{ho}^* = \frac{2\sigma}{\Delta G} \quad (9)$$

$$r_{he}^* = \frac{2\sigma_{ic}}{\Delta G} \quad (10)$$

where  $\Delta G$  is the unit volume free energy required for the formation of a new phase,  $\sigma$  and  $\sigma_{ic}$  are, respectively, the unit interface free energies between the liquid phase and the nucleation site during homogeneous and heterogeneous nucleations.

The physical meaning of  $\sigma$  and  $\sigma_{ic}$  is the same, thus resulting in the same critical nucleation radius during homogeneous and heterogeneous nucleations. However, the heterogeneous nucleation site is a part of the nucleation sphere. It implies that TiN particles require few atoms before reaching the critical nucleation radius, and thus, the resistance of heterogeneous nucleation decreases. Zheng et al. [38] propounded that 80% TiN inclusions are in the heterogeneous nucleation mode during solidification. Although the volume of nucleation sites for TiN increases by heterogeneous nucleation, there is a threshold value in composite inclusions during the solidification of the molten steel when the cooling rate is constant. This phenomenon can be explained by the diffusion coefficient of N. With the increase in TiN size, more N is required. The time for TiN growth is limited as the cooling rate is constant. Thus, the

diffusion distance of N is confined, and it is not possible for composite inclusions of TiN to grow unrestrainedly.

### 3.3 Morphologies of TiN Particles

In the study on crystal orientation relationship, Yong et al. [39] proved that carbon nitride particles are spherical at the beginning of the formation process. The effects of interface energy induced by carbon nitride particles become insignificant after the growth process; thus, the stage at the interface acts as the preferential adhering sites of new diffused atoms. According to the theory developed by Jackson et al. [40], when the value of dimensionless entropy of a certain phase is smaller than 2, the phase will grow with a non-faceted morphology or a rough interface. However, if the value of dimensionless entropy is larger than 2, this phase will grow with a regular faceted morphology or a smooth interface. The dimensionless entropy for TiN is about 2.5, which is larger than the threshold value of 2, and thus, TiN generally presents faceted morphology [2, 24]. TiN possesses a face-centered cubic (FCC) crystal structure and different crystal planes possess different surface energies and grow at different rates. The growth rate of crystal planes with low surface energies (which control the shape of TiN particles) is generally very slow. According to the Woolf curve [41], cuspidal points representing the minimum surface energy exist in the directions of  $\langle 100 \rangle$  and  $\langle 111 \rangle$  of an FCC crystal; therefore, the  $\{100\}$  and the  $\{111\}$  crystal planes can be regarded as its equilibrium crystal plane. When the  $\{111\}$  crystal plane controls the growth of TiN, eight  $\{111\}$  crystal planes form an octahedron. Similarly, six  $\{100\}$  crystal planes form a cube when the growth of TiN particles is controlled by the  $\{100\}$  crystal plane.

In order to examine the precipitation morphologies of TiN particles, the cross-sectional morphologies on the surface and at the core of the continuous casting slabs are displayed in Fig. 5. Four different shapes, such as square, rectangle, triangle, and trapezoid, are noticed in cross-sectional morphologies of TiN particles. Ten SEM images with the same magnification have been used to determine the average size of TiN particles based on number density using JMATPRO software, and almost 50–70 TiN particles have been taken from each specimen to ensure a reliable analysis. Figure 6 illustrates the size distribution of TiN particles on the surface and at the core of the continuous casting slabs. The unimodal size distribution is observed for TiN particles. It is observed that TiN particles on the surface mainly concentrate within  $6.0 \mu\text{m}$ , whereas the section of TiN particles at the core of the continuous casting slabs is  $\sim 8.0 \mu\text{m}$ . The average sizes of TiN particles on the surface and at the core of the continuous casting slabs are  $4.3 \mu\text{m}$  and  $7.4 \mu\text{m}$ , respectively,

**Fig. 5** Cross-sectional morphologies of TiN in **a**, **b** surface and **c**, **d** core in the casting slabs

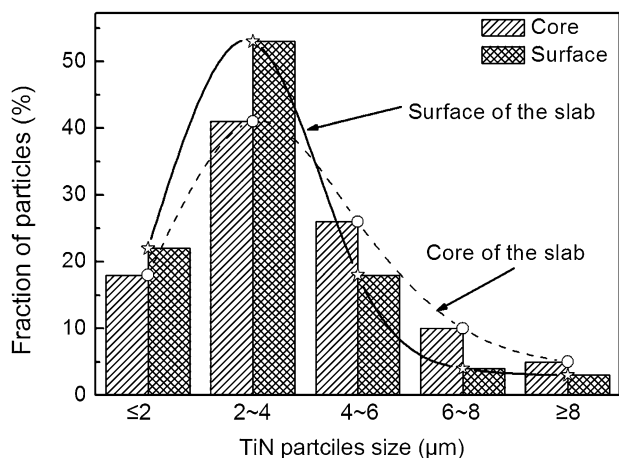
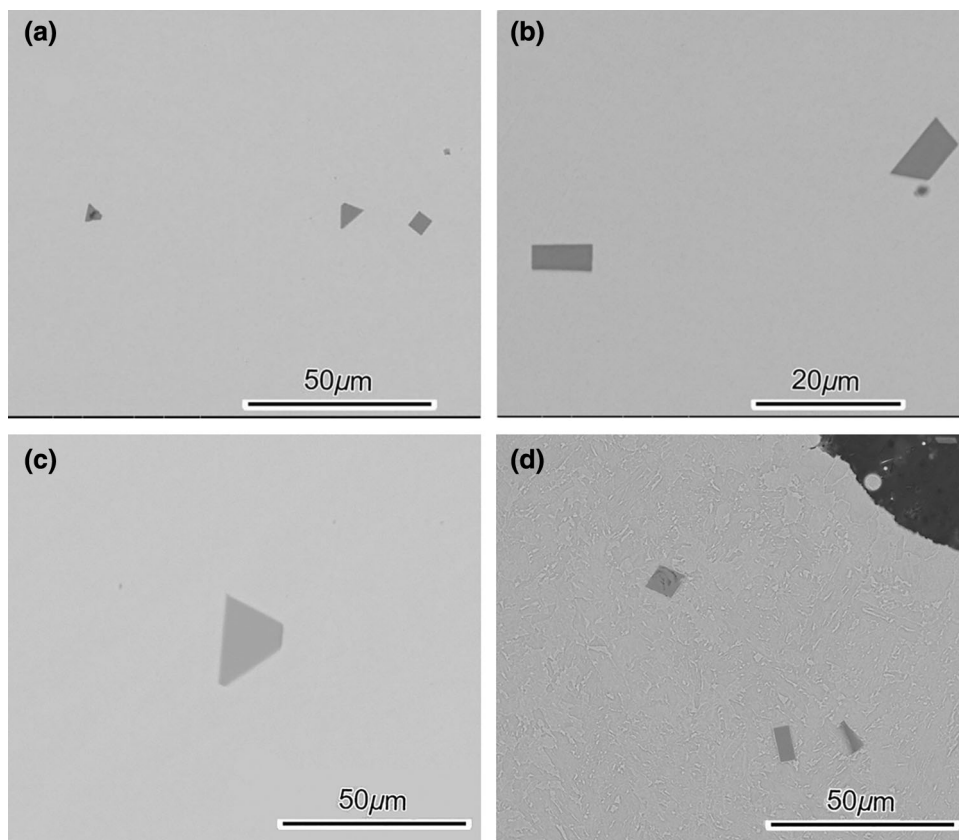


**Fig. 6** Size distributions of the TiN particles at the surface and core in the continuous casting slabs

signifying that the size of TiN particles at the core is larger than that on the surface in the continuous casting slabs. The statistical results in the dimensions of the TiN particles from the surface and the core in the continuous casting slabs are consistent with the calculation in Fig. 3, both demonstrating that the dimension of TiN particles decreases with the increase in the cooling rate.

The possible reason for different TiN particle sizes can be attributed to different cooling rates across the slabs

during the continuous casting process. Based on industrial data, the cooling rates on the surface and at the core of the slab are about 500 °C/min and about 10 °C/min, respectively. Precipitation nucleation is a type of diffusion transformation and depends on the diffusions of N, Ti, and Nb atoms. It is well known that atomic diffusion manifests a positive correlation with temperature. The instantaneous temperature at the core position of the slabs is higher due to the relatively slow heat transfer, thus resulting in efficient nucleation and growth of TiN particles. On the contrary, the precipitation and growth behavior of TiN particles on the surface of the slab are limited due to the fast heat transfer towards the environment. Normally, composite carbonitrides of microalloying elements manifest excellent thermal stability due to their complex chemical compositions [39]. However, the size of TiN particles increases from the surface to the core of the slab because TiN particles have a relatively simple chemical composition, thus resulting in poor thermal stability. In addition, the actual size of TiN particles is smaller than the calculated values, which can be explained by excluding the reactions between Ti and O, Al, and N.

Figure 7 displays the three-dimensional morphologies of TiN particles at the core of the slabs. The top view and the side view are both recorded by FIB-SEM. It is noticeable that only the basement of TiN particles is retained after

**Fig. 7** Three-dimensional morphology of TiN particles: **a** top view graph and **b** side view graph

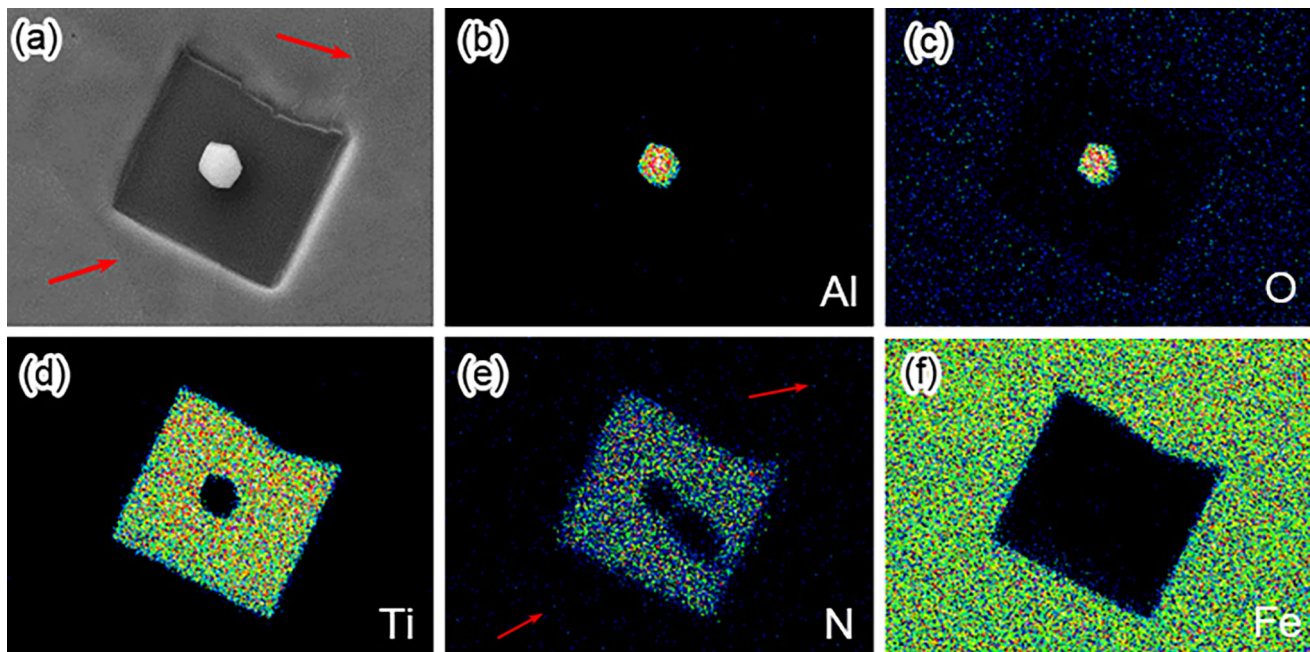
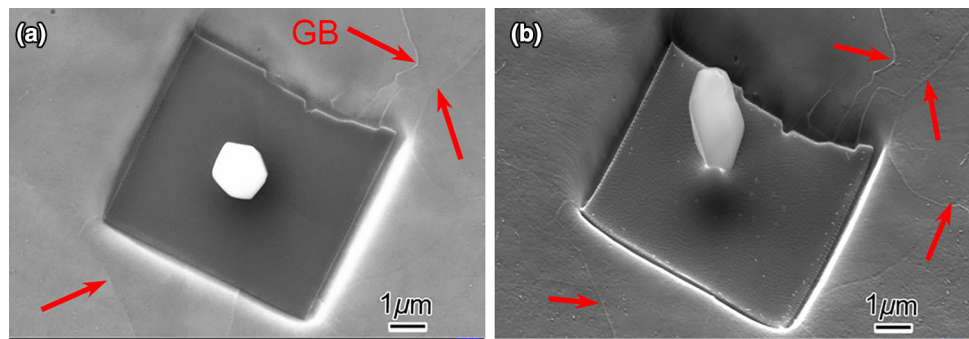


**Fig. 8** Corresponding selected area elemental mapping result of the  $\text{Al}_2\text{O}_3$ -TiN composite inclusion

electrolytic etching. The nucleus of heterogeneous nucleation for TiN particles is of rice-granule shape with a hexagonal cross section, and its diameter is about  $1.8 \mu\text{m}$ . The length and the width of rectangular TiN particles are  $\sim 6.36 \mu\text{m}$  and  $\sim 5.82 \mu\text{m}$ , respectively. The reason for the formation of large-sized TiN (in comparison to other microalloyed carbonitrides) can be explained by its higher precipitation temperature. It is well known that larger TiN particles have little precipitation strength contribution to steels. Moreover, larger TiN particles deteriorate the toughness of steels. Furthermore, some grain boundaries are found around TiN precipitates. It can be inferred that these TiN precipitates are mainly formed at grain boundaries and act as the heterogeneous sites for ferrite formation during solidification. The observed TiN particles found adhering to heterogeneous sites also

demonstrate that it is easier to happen for heterogeneous nucleation than homogeneous nucleation during the TiN formation, which is in accord with the introduction in Sect. 3.2.

Figure 8 presents the results of selected area elemental mapping.  $\text{Al}_2\text{O}_3$  particles are the nucleus of heterogeneous nucleation for TiN particles.  $\text{Al}_2\text{O}_3$  particles act as the deoxidizing agent in the steel to provide nucleation sites for the formation of TiN particles. In addition, some scholars also found an intermediate transitional phase of  $\text{Al}_2\text{TiO}_5$  in  $\text{Al}_2\text{O}_3$ -TiN composite inclusions [8]. Except for  $\text{Al}_2\text{O}_3$  particles,  $\text{MgO/MgS}$  or  $\text{MnS}$  also play the same role in heterogeneous nucleation of TiN particles. Furthermore, Ti only aggregates in TiN precipitates and no enrichment of Ti is detected at grain boundaries. This is because Ti is consumed by TiN precipitates and the solid-solution in

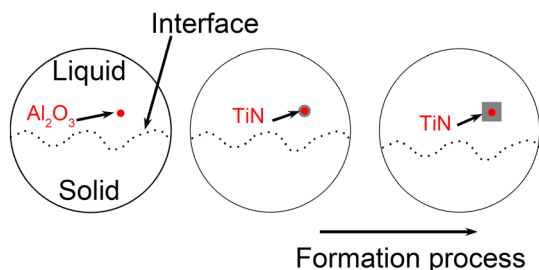


**Fig. 9** Schematic of the formation mechanism of TiN with  $\text{Al}_2\text{O}_3$

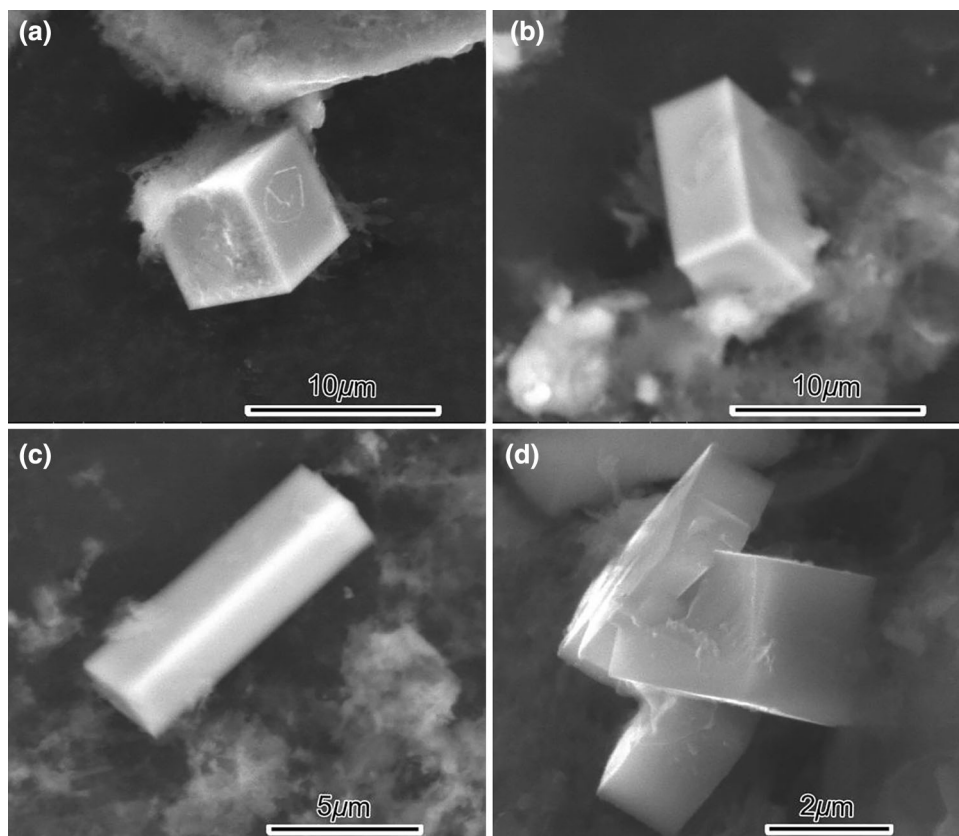
ferrite. However, N atoms are detected at grain boundaries (Fig. 8e), revealing that the amount of N is relatively more than Ti. As the affinity of N with Ti is stronger than that with C, TiC can not be formed when N exists. Moreover, O is distributed dispersedly in the matrix region, implying that  $\text{Al}_2\text{O}_3$  particles for the heterogeneous nucleation of TiN appear in the original melt before solidification.

Figure 9 depicts the formation mechanism of TiN at the  $\text{Al}_2\text{O}_3$  core. During solidification, as the equilibrium distribution coefficients of Ti and N are both less than unity, solid solutions of Ti and N atoms are expelled to the liquid, at or ahead of the interface between solid and liquid. Ti and N atoms at or ahead of the interface gradually accumulate and reach a critical value, and thus, TiN is formed from the melt. Simultaneously, the appearance of  $\text{Al}_2\text{O}_3$  particles is

easily found. In comparison to homogeneous nucleation, the rate of undercooling in heterogeneous nucleation is much lower, and thus, the latter pattern dominates the formation mechanism of TiN precipitates.

Figure 10 presents the spatial tridimensional morphologies of TiN particles. TiN particles possess both square and cluster morphologies, and the square morphology is found to be predominant. Sharp edges are observed in these TiN particles, and their sizes are about 5–10  $\mu\text{m}$ . The spatial tridimensional morphology (octahedron or cube) of TiN generally depends on its formation surroundings. The octahedron morphology of TiN is often observed in TiN coatings fabricated by chemical vapor deposition, whereas cube-shaped TiN particles are mainly formed during metallurgical processes caused by turbulence and the collision mechanism of Stokes in the molten steel [41]. Due to the dispersive distribution of TiN particles in the tested steel, various cross-sectional morphologies are noticed (Fig. 5). The reason for cube-shaped TiN formation can be attributed to interface energy. The interface energy during solidification is determined by the atomic density of crystal planes. The bounded plane of faceted phases possesses the lowest interface energy during solidification. The atomic density of the FCC {100} structure for TiN precipitates is higher than that of FCC {111}. TiN precipitates are of cubic shape when the

**Fig. 10** Spatial tridimensional morphologies of TiN particles





interface is bounded by the secondary close-packed (100) plane. It is found that the preferential plane for TiN precipitates in the tested steel is {100}. In addition, impurities in molten metals affect the growth behavior of the specific planes and cause a significant change in the final crystal structure.

#### 4 Conclusions

In the present study, thermodynamics and dynamics equations were used to analyze the precipitation behavior of TiN particles under homogeneous and heterogeneous nucleation conditions of low-carbon high-strength steel with 0.11 wt% Ti. In addition, the three-dimensional and the spatial tridimensional morphologies of TiN were characterized by a focused ion beam scanning electron microscope. The following main conclusions are obtained.

1. TiN particles precipitate both in solid and liquid phases from the solid–liquid phase region during the solidification process, and preferential precipitation is observed in the solid phase.
2. The size of TiN particles decreases with the increasing cooling rate during the casting process, and it is verified by the increasing TiN particle size from the surface (4.3  $\mu\text{m}$ ) to the core (7.6  $\mu\text{m}$ ) in the continuous casting slabs.
3.  $\text{Al}_2\text{O}_3$  particles, as the deoxidizing product in the tested steel, provide nucleation sites for the heterogeneous nucleation of TiN particles.
4. TiN particles possess inerratic facet morphologies (such as squares and clusters), and the square morphology is predominant. In addition, the preferential plane for TiN precipitates in the tested steel is {100}.

**Acknowledgements** The authors gratefully acknowledge the financial supports from The National Natural Science Foundation of China (NSFC) (No. 51771139).

#### References

1. Tian X, Zhu G M, Kang Y L, Zhang Y K, and Tan J M. *Chin J Eng* **37** (2015) 42.
2. Zhu M, Xu G, Zhou M X, and Hu H J. *J Univ Sci Technol Wuhan* **3** (2019) 692.
3. Gan X L, Xu G, Zhao G, Zhou M X, and Cai Z. *J Univ Sci Technol Wuhan* **5** (2018) 1193.
4. Hu Z W, Xu G, Yang H L, Zhang C, and Yu R. *J Mater Eng Perform* **23** (2014) 4216.
5. Yang H L, Xu G, Wang L, Yuan Q, and He B. *Met Sci Heat Treat* **59** (2017) 8.
6. Wang X S, Liang F, Zeng Y P, and Xie X S. *Acta Metall Sin* **41** (2005) 1272.

7. Fu J, Zhu J, Di L, Tong F S, Liu D L, and Wang Y L. *Acta Metall Sin* **36** (2000) 801.
8. Sui Y F, Sun G D, Zhao Y, Wang C G, Guo M, and Zhang M. *J Univ Sci Technol Beijing* **36** (2014) 1174.
9. Gan X L, Yuan Q, Zhao G, Hu H J, Tian J Y, and Xu G. *Steel Res Int.* <https://doi.org/10.1002/srin.201900040>
10. Yan W, Shan Y Y, and Yang K. *Metall Mater Trans A* **37** (2006) 2147.
11. Mi G F, and Nan H Y. *J Iron Steel Res* **18** (2011) 49.
12. Kabo E, and Ekberg A. *Wear* **253** (2002) 26.
13. Zhang J M, Zhang J F, Yang Z G, Li S X, Hui W J, and Wong Y Q. *Acta Metall Sin* **40** (2004) 846.
14. Hui W J, Dong H, Weng Y Q, Shi J, Nie Y H, Chu Z M, and Chen Y B. *Acta Metall Sin* **40** (2004) 561.
15. Levy B S, Van Tyne C J, *J Mater Eng Perform* **17** (2008) 842.
16. Chung K, Ma N, Kim D, and Yoo D. *Int J Plast* **27** (2011) 1485.
17. Shinsho Y, and Nozaki T. *Wire J Int* **9** (1988) 145.
18. Jiang Y D, Lei J L, Zhang J, Xiong R, Zou F, and Xue Z L. *J Surf Eng Mater Adv Technol* **3** (2013) 283.
19. Zhao D W, Bao Y P, Wang M, Ma W J, and Su L C. *Spec Steel* **33** (2012) 7.
20. Chen C Y, Chen C C, and Yang J R. *Mater Charact* **88** (2014) 69.
21. Misra R, Nathani H, and Hartmann J E. *Mater Sci Eng A* **394** (2005) 339.
22. Duan X G, Cai Q W, and Wu H B. *Acta Metall Sin* **47** (2011) 251.
23. Yi H L, Liu Z Y, Wang G D, and Wu D. *Iron Steel Res Int* **17** (2010) 54.
24. Liu Q, Peter H, Zhang H W, Wang Q, Jonsson P, and Nakajima K. *ISIJ Int* **52** (2012) 2288.
25. Misra R D K, Nathani H, Hartmann J E, and Siciliano F. *Mater Sci Eng A* **394** (2005) 339.
26. Reip C P, Shanmugam S, and Misra R D K. *Mater Sci Eng A* **424** (2006) 307.
27. Fan L, Wang T L, Fu Z B, Zhang S M, and Wang Q F. *Mater Sci Eng A* **607** (2014) 559.
28. Liu Y, Zhang L F, Duan H J, Zhang Y, Luo Y, and Conejo A N. *Metall Mater Trans A* **47A** (2016) 3015.
29. Michelic S K, Loder D, Reip T, Barani A A, and Bernhard C. *Mater Charact* **100** (2015) 61.
30. Chen J X, *Common Chart Data Manual for Steel Making*, Metallurgical Industry Press, Beijing (1984), p 67.
31. Zeng X G. *J Univ Sci Technol Beijing* **31** (2009) 145.
32. Takashi M, and Masafumi Z. *Tsutsu-to-Hagané* **99** (2013) 17.
33. Jiang Y D, Xue Z L, Wu J, Gui M W, and Zheng Y F. *J Univ Sci Technol Wuhan* **33** (2010) 258.
34. Pelton A D, Eriksson G, and Bale C W. *Metall Mater Trans A* **6** (2017) 3113.
35. Zhao J P, Liu L, Fan J W, and Wang L. *Iron Steel Vanadium Titan* **37** (2016) 116.
36. Hiroki G, Ken-ichi M, Wataru Y, and Kazuaki T. *ISIJ Int* **35** (1995) 708.
37. Wang X H, *Iron and Steel Metallurgy*, Higher Education Press, Beijing (2007), p 286.
38. Zheng W, Qu Y, Fu X H, Li G Q, and Wu Z H. *J Univ Sci Technol Wuhan* **40** (2017) 161.
39. Yong Q L, *Microalloyed Steels Physical and Mechanical Metallurgy*, China Machine Press, Beijing (1989).
40. Jackson K A. *J. Cryst Growth* **264** (2004) 519.
41. Qin S, *Fundamentals of Crystallography*, Peking University Press, Beijing (2004), p 146.

**Publisher's Note** Springer Nature remains neutral with regard to jurisdictional claims in published maps and institutional affiliations.